PAPER

Comparative study on La-promoted Ni/γ-Al₂O₃ for methane dry reforming – spray drying for enhanced nickel dispersion and strong metal–support interactions†

N. Pegios,[a] V. Bliznuk,[b] S. Prünte,[c] J. M. Schneider,[c] R. Palkovits [ID] *[a] and K. Simeonov[a]

Dry reforming of methane (DRM) enables an efficient utilization of two abundant greenhouse gases by converting them into syngas, a versatile feedstock for chemical synthesis. Aiming for high catalyst performance and enhanced coke resistance, different preparation techniques of La-promoted Ni/γ-Al₂O₃ catalysts for DRM were compared facilitating structure–performance correlations. The studied synthesis techniques comprehend incipient wetness impregnation and co-precipitation as well as alternative techniques such as spray drying. All catalysts were fully characterized before and after reaction by N₂-physisorption, XRD, H₂-TPR and STEM-EDX elemental mapping. Additionally, a thorough investigation of carbon deposits has been carried out by TGA/DSC and STEM-EDX, respectively. The different preparation techniques led generally to very different physical properties, structure, chemical species and anti-coking properties of the catalyst. However, some catalysts with similar physicochemical characteristics differed in catalytic performance and coking resistance. Superior catalytic performance could be reached for catalysts prepared by spray drying and related to excellent Ni dispersion, strong metal–support interaction and very low coke formation of only 2.7% of the catalyst weight. After 6 h time on stream only minor sintering occurred, with few Ni nanoparticles up to 10 nm.

1. Introduction

Concerns over CO_2 emissions have substantially increased over the past few decades. CO_2 is a very stable molecule and is considered to be among the main greenhouse gases leading to global warming.[1] Currently, anthropogenic emissions of CO_2 in the atmosphere are estimated to contribute around 60% of the total of all the anthropogenic gases.[2] In the future they are expected to rise further due to the ongoing combustion of fossil fuels. Almost all CO_2 produced from combustion processes is emitted into the atmosphere where it gradually accumulates.[1] Besides CO_2, CH_4 is considered to be another major greenhouse gas.[3,4] Therefore, there is much interest in the utilization of CO_2 and CH_4. A promising approach to carbon capture and utilization (CCU) presents dry reforming of methane (DRM) (eqn (1)). The process makes use of the two abundantly available greenhouse gases by converting them into syngas, a versatile feedstock for chemical synthesis. DRM has attracted considerable attention in recent years since it produces high purity syngas compared to coal and biomass.[5,6] Different classes of catalysts have shown potential to deliver reasonable and economically feasible results for DRM.[7–9] Even though noble metal catalysts exhibit superior activity and stability amongst others,[10–14] their scarcity and price make them unattractive. On the other hand, nickel based catalysts are a commonly proposed alternative due to their high activity, low cost and the abundant supply of nickel compared to noble metals. The main challenge nickel based catalysts face is deactivation, occurring *via* sintering and carbon deposition.[15–17] Carbon deposits are formed mainly *via* CH_4 cracking (eqn (2)) and CO disproportion (Boudouard reaction) (eqn (3)).[18] Sintering on the other hand, although found to have less direct influence on activity and stability of the catalyst compared to carbon deposition, significantly promotes coking.[15,17] Many efforts have been made to improve the carbon deposition resistance of nickel based catalysts. Amongst them, rare earth metals such as La,[19–21] Ce,[22,23] and Zr,[24] can reduce carbon deposition and improve sintering resistance. Lanthanides favor metal dispersion,[25,26] and strengthen CO_2 adsorption on the support.[27] The presence of oxy-carbonates over La_2O_3 facilitates coke removal since they seem to act as a dynamic oxygen pool.[28]
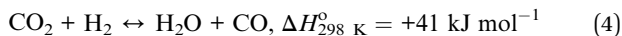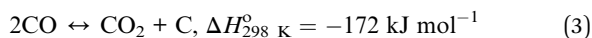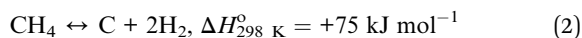
[a]Department of Heterogeneous Catalysis, Chemical Technology (ITMC), RWTH Aachen University, Worringerweg 2, Aachen 52074, North Rhine-Westphalia, Germany. E-mail: Palkovits@itmc.rwth-aachen.de

[b]Department of Electrical Energy, Metals, Mechanical Construction & Systems (EEMMeCS), Group Metals Science & Technology, Tech Lane Ghent Science Park – Campus A, Technologiepark 903, B-9052 Gent, Belgium

[c]Materials Chemistry, RWTH Aachen, Kopernikusstr. 16, Aachen 52074, Germany

$$CO_2 + CH_4 \leftrightarrow 2CO + 2H_2, \Delta H^o_{298\ K} = +247\ kJ\ mol^{-1} \quad (1)$$

$$CH_4 \leftrightarrow C + 2H_2, \Delta H^o_{298\ K} = +75\ kJ\ mol^{-1} \quad (2)$$

$$2CO \leftrightarrow CO_2 + C, \Delta H^o_{298\ K} = -172\ kJ\ mol^{-1} \quad (3)$$

$$CO_2 + H_2 \leftrightarrow H_2O + CO, \Delta H^o_{298\ K} = +41\ kJ\ mol^{-1} \quad (4)$$

Therefore, this study focusses on Ni on γ-Al_2O_3 promoted with lanthanum. La is commonly used to form perovskite-like structures. Whereas in this study, La is envisioned as a textural promoter to enhance nickel dispersion and to accelerate carbon deposits removal, respectively. Numerous studies, both experimental,[29–31] and computational (DFT),[31–34] suggest that a reduced Ni-nanoparticle size enhances activity and minimizes carbon formation. Especially a Ni particle size of less than 5 nm appears advantageous for coke-resistant catalysts.[34] Despite intensive research in the field, the influence of preparation techniques on catalyst properties and the associated performance in DRM has been investigated rarely. In order to address these, we compared seven La-promoted Ni/γ-Al_2O_3 catalysts prepared by a wide range of different synthetic techniques, all aiming at obtaining catalysts with high specific surface area and high active metal dispersion. The methods comprehend incipient wetness impregnation and co-precipitation as they are commonly used in the literature providing decent catalytic results towards DRM. Spray drying was also utilized since the achieved Ni dispersion is excellent. To the best of our knowledge, spray drying has been rarely used for Ni-based catalysts in DRM. Additionally, we modified spray drying and co-precipitation by combining them with physical mixture and an ethanol suspension approach. In this way, we could also evaluate the influence of ethanol as a suspension medium on the properties of the catalyst. Furthermore, feed ratio of $CO_2 : CH_4 = 2 : 1$ was utilized since higher partial pressure of CO_2 in the feed was found to suppress sintering and coke formation.[35,36] We focused on structural and physicochemical characterization of these materials before and after testing, as well as their activity and stability in DRM. Together with a throughout analysis of carbon deposits, a correlation between the impact of preparation techniques on catalyst properties and their catalytic performance and coking behavior became evident.

2. Experimental

2.1. Catalyst preparation

Seven different preparation techniques were applied to synthesize La (25 wt%)-promoted Ni (10 wt%)/γ-Al_2O_3 catalysts (Table 1). The catalyst denoted as IW3M was synthesized by the standalone preparation technique of incipient wetness impregnation, utilizing all 3 metals. 0.5 g of $Ni(NO_3)_2 \cdot 6H_2O$ (Sigma Aldrich, ≥ 97.0) and 0.74 g of $La(NO_3)_3 \cdot 6H_2O$ (Sigma Aldrich, $\geq 99.9\%$) were dissolved in distilled water to form a saturated solution which was impregnated to incipient wetness on 1.0 g of γ-Al_2O_3 powder (Sasol, $A_{BET} = 160\ m^2\ g^{-1}$, $V_P \geq 0.45\ mL\ g^{-1}$). The obtained material was dried overnight at

80 °C and calcined at 800 °C in air for 8 h with a ramping rate of 10 K min^{-1}. The same drying/calcination parameters were applied to all catalysts of the series.

The catalyst denoted as SD3M was synthesized by the standalone preparation technique of spray drying, utilizing a 3-metal solution. 0.5 g of $Ni(NO_3)_2 \cdot 6H_2O$, 0.74 g of $La(NO_3)_3 \cdot 6H_2O$ and 7.36 g of $Al(NO_3)_3 \cdot 9H_2O$ (Sigma Aldrich, ≥ 98.0) were dissolved in 230 mL distilled water to form a solution of 0.1 M concentration based on the total amount of metal nitrates. The solution was then fed with a constant rate of 3 mL min^{-1} into a spray dryer (BÜCHI Mini-Spray-Dryer B-290) with N_2 as carrier gas at 4 mL min^{-1} and air as drying gas at 550 L min^{-1} at 140 °C. The obtained material was dried overnight and calcined.

The catalyst denoted as CP3M was synthesized by co-precipitation, utilizing a 3-metal solution. 0.5 g of $Ni(NO_3)_2 \cdot 6H_2O$, 0.74 g of $La(NO_3)_3 \cdot 6H_2O$ and 7.36 g of $Al(NO_3)_3 \cdot 9H_2O$ were dissolved in 250 mL distilled water and heated to 50 °C. 185 mL of 0.4 M NaOH were added and stirred for 30 min. The formed precipitate was cooled to room temperature, filtered and washed multiple times with distilled water. The obtained material was dried and calcined as already indicated.

The catalysts denoted as SD + SolidMix and SD + suspension were synthesized by applying the combined techniques of spray drying/physical mixture and spray drying/ethanol suspension, respectively. 2.0 g of $Ni(NO_3)_2 \cdot 6H_2O$ and 2.96 g of $La(NO_3)_3 \cdot 6H_2O$ were dissolved in 137 mL distilled water to form a solution of 0.1 M concentration based on the total amount of metal nitrates. The rest of the procedure is identical to the one applied to SD3M catalyst. After calcination, half of the collected material was physically mixed with 2 g of γ-Al_2O_3 to obtain SD + SolidMix catalysts, whereas the other half was suspended in ethanol with 2 g of γ-Al_2O_3 and after agitation for 30 minutes dried to produce the SD + suspension catalyst. Both materials were finally calcined.

The catalysts denoted as CP + SolidMix and CP + suspension were synthesized by combining co-precipitation and physical mixture, and co-precipitation- and ethanol suspension, respectively. 2.0 g of $Ni(NO_3)_2 \cdot 6H_2O$ and 2.96 g of $La(NO_3)_3 \cdot 6H_2O$ were dissolved in 67 mL of distilled water and heated to 50 °C. 225 mL of 0.2 M NaOH were added and stirred for 30 min. The formed precipitate was quenched to room temperature, filtered and washed multiple times with distilled water. The obtained material was dried overnight and calcined. Half of the collected material was physically mixed with 2 g of γ-Al_2O_3 to obtain the CP + SolidMix catalyst, while the other half was suspended in ethanol with 2 g of γ-Al_2O_3, agitated for 30 minutes and dried to obtain the CP + suspension catalyst. Both materials were finally calcined.

2.2. Catalyst characterization

The total surface area was determined by the BET method based on N_2-physisorption capacity using a Micromeritics ASAP 2020 at 77.35 K. Prior to analysis, all the samples were degassed at 600 K under pure He flow. ICP-OES was performed on an ICP Spectroflame D by Spectro. The phase composition of the catalysts was evaluated by X-ray diffraction measurements

Table 1 Catalyst preparation overview

Catalyst	Preparation technique	Step 1	Step 2	Step 3
IW3M	Incipient wetness impregnation	$Ni(NO_3)_2 \cdot 6H_2O$ and $La(NO_3)_3 \cdot 6H_2O$ dissolved in water and impregnated on γ-Al_2O_3	Dried overnight[a] and calcined[b]	—
SD3M	Spray drying	$Ni(NO_3)_2 \cdot 6H_2O$, $La(NO_3)_3 \cdot 6H_2O$ and $Al(NO_3)_3 \cdot 9H_2O$ dissolved in water and then spray dried		—
CP3M	Co-precipitation	$Ni(NO_3)_2 \cdot 6H_2O$, $La(NO_3)_3 \cdot 6H_2O$, $Al(NO_3)_3 \cdot 9H_2O$ dissolved in water and mixed with $NaOH_{(aq)}$. Filtered and washed		—
SD + SolidMix	Spray drying/ physical mixture	$Ni(NO_3)_2 \cdot 6H_2O$ and $La(NO_3)_3 \cdot 6H_2O$ dissolved in water and then spray dried		Physical mixture with γ-Al_2O_3 and calcined[b] second time
SD + suspension	Spray drying/ ethanol suspension	$Ni(NO_3)_2 \cdot 6H_2O$ and $La(NO_3)_3 \cdot 6H_2O$ dissolved in water and then spray dried		Ethanol suspension with γ-Al_2O_3, dried[a] and calcined[b] second time
CP + SolidMix	Co-precipitation/ physical mixture	$Ni(NO_3)_2 \cdot 6H_2O$ and $La(NO_3)_3 \cdot 6H_2O$ dissolved in water and mixed with $NaOH_{(aq)}$. Filtered and washed		Physical mixture with γ-Al_2O_3 and calcined[b] second time
CP + suspension	Co-precipitation/ ethanol suspension	$Ni(NO_3)_2 \cdot 6H_2O$ and $La(NO_3)_3 \cdot 6H_2O$ dissolved in water and mixed with $NaOH_{(aq)}$. Filtered and washed		Ethanol suspension with γ-Al_2O_3, dried[a] and calcined[b] second time

[a] Overnight at 80 °C. [b] At 800 °C in air for 8 h (10 K min^{-1}).

(XRD) performed with a Siemens D5000 X-ray diffractometer with Cu K_α ($\lambda = 0.15409$ nm, 40 kV, 40 mA) radiation and a scanning step width of 0.02°. Temperature programmed reduction with H_2 (H_2-TPR) was performed on a TPDRO 1100 Porotec unit using thermal conductivity detection. Thermogravimetric analysis and differential scanning calorimetry (TGA/DSC) were performed on a Netzsch STA 409C/CD appliance. The temperature was increased starting from 25 °C to 1000 °C with a heating rate of 5 K min^{-1}. The morphology of both fresh and spent catalysts was characterized by a transmission electron microscope (TEM) JEOL JEM-2200FS equipped with Schottky type field emission electron emitter, in column omega-type electron energy filter, objective lens aberrations corrector CETCOR (CEOS GmbH), a slow scan CCD camera Gatan for high resolution (HR) TEM, a scanning transmission electron mode (STEM) and an energy dispersive X-ray (EDX) spectrometer JED-2300 (Jeol). Surface chemistry was investigated by X-ray spectroscopy (XPS) using a JEOL JAMP 9500F equipped with a non-monochromatic Al Kα X-ray source. Fresh and spent IW3M and SD3M catalysts were carefully pressed onto Sn-foil to embed the powders in a conductive medium. Charge calibration was carried out by using the aliphatic C 1s signal at 285.0 eV. However, shifting the energy scale according to the signals of the dielectric powders lead to an off-set of signals stemming from the Sn-foil, which were identified by their energetic distance to the Sn $3d_{5/2}$-signal and a comparison with signals of a plain Sn-foil. Detailed spectra were recorded with a pass energy of 20 eV of the detector, 0.05 eV step size and 20 recording cycles. CASA XPS was used for data analysis where mixed Gaussian–Lorentzian (30–70%) signals and Shirley backgrounds were applied for data fitting.

2.3. Catalytic testing

A plug-flow fixed-bed quartz tube reactor, with an internal diameter of 6 mm inside a tubular furnace was used. The furnace was regulated by a K-type thermocouple attached to it. The height of the bed was kept constant at 1 cm. All catalysts were firstly reduced *in situ* in 90 mL min^{-1} pure H_2 flow at 800 °C for 2 h with the exception of SD3M which was reduced for 3 h. All reactions were carried out at 800 °C with a gas hourly space velocity of 35 000 h^{-1} and feed ratio CO_2 : CH_4 of 2 : 1 under atmospheric pressure. 10% N_2 (v/v) of the reactant flow was introduced as an internal standard to account for volume expansion during reaction. The outlet gases were analyzed by an online gas chromatographer (GC) Bruker 400 GC Series equipped with two thermal conductivity (TCD) and one flame ionization (FID) detectors. The outlet gases were first allowed to pass through a cold trap to remove the produced water and then through a dryer/absorber containing Drierite™ to remove humidity before entering the GC.

Conversions and selectivities were calculated through the equations

$$\text{Conv.}_{CH_4}(\%) = \frac{(F_{CH_4,in} - F_{CH_4,out})\ (mL\ min^{-1})}{F_{CH_4,in}\ (mL\ min^{-1})} \times 100, \quad (5)$$

$$\text{Conv.}_{CO_2}(\%) = \frac{(F_{CO_2,in} - F_{CO_2,out})\ (mL\ min^{-1})}{F_{CO_2,in}\ (mL\ min^{-1})} \times 100, \quad (6)$$

$$R_{CH_4}(mol\ g_{cat.}^{-1}\ s^{-1}) = \frac{CH_{4,in}\ (g\ L^{-1})CH_{4,in}(L\ s^{-1})\text{conv.}_{CH_4}}{100\ 16.04\ g_{cat.}}, \quad (7)$$

$$R_{CO_2}(mol\ g_{cat.}^{-1}\ s^{-1}) = \frac{CO_{2,in}\ (g\ L^{-1})CO_{2,in}(L\ s^{-1})\text{conv.}_{CO_2}}{100\ 44.01\ g_{cat.}}, \quad (8)$$

$$\text{Sel.}_{H_2}(\%) = \frac{F_{H_2,out}\ (mL\ min^{-1})}{F_{CH_4,in} - F_{CH_4,out}\ (mL\ min^{-1})} \times 0.5 \times 100, \quad (9)$$

$$\text{Sel.}_{CO}(\%) = \frac{F_{CO,out}\ (mL\ min^{-1})}{(F_{CH_4,in} - F_{CH_4,out}) + (F_{CO_2,in} - F_{CO_2,out})\ (mL\ min^{-1})} \times 100, \quad (10)$$

$$\frac{H_2}{CO} = \frac{mol_{H_2,out}}{mol_{CO,out}}, \quad (11)$$

where Conv._{CH_4} and conv._{CO_2} are the conversions of methane and carbon dioxide as percentages, respectively, and Sel._{H_2} and Sel._{CO} are the selectivities to hydrogen and carbon monoxide as percentages, respectively. $F_{CH_4,in}$, $F_{CH_4,out}$ and $F_{CO_2,in}$, $F_{CO_2,out}$ are the inlet and outlet flows of methane and carbon dioxide (mL min^{-1}), respectively, whereas $F_{H_2,out}$ and $F_{CO,out}$ are the respective flows of hydrogen and carbon monoxide at the reactor outlet (mL min^{-1}).

3.   Results and discussion

3.1.   Fresh catalyst characterization

Lanthanum (25 wt%) promoted nickel (10 wt%) catalysts supported on alumina were prepared using the standalone preparations techniques of incipient wetness impregnation (IW3M), co-precipitation (CP3M) and spray drying (SD3M), as well as the combined techniques of spray drying/physical mixture (SD + SolidMix), spray drying/ethanol suspension (SD + suspension), co-precipitation/physical mixture (CP + SolidMix) and co-precipitation/ethanol suspension (CP + suspension) of the different salts, respectively. All calcined catalysts exhibited specific surface areas around 98–138 m^2 g^{-1} except the one of the catalyst prepared by spray drying (SD3M) that was only 9.8 m^2 g^{-1} (Table 2).

XRD measurements were also carried out (see ESI†) for all freshly calcined catalysts. IW3M, SD3M and CP3M exhibited very low crystallinity, which was not expected due to the harsh calcination conditions of 800 °C for 8 h. Literature reports suggest that γ-Al$_2$O$_3$ appears at temperatures between 350 and 1000 °C when formed from crystalline[37] or amorphous[38] precursors. More studies should be performed in order to understand better this observation. XRD patterns of these three catalysts showed reflections with relatively low intensity related to γ-Al$_2$O$_3$ as well as NiAl$_2$O$_4$, respectively. The other materials possessed a higher degree of crystallinity emphasized by more intense reflexes corresponding to γ-Al$_2$O$_3$ and NiAl$_2$O$_4$. More specifically, all four materials exhibited distinguishable reflexes of γ-Al$_2$O$_3$ (more pronounced at 32.7°, 39.5°, 45.5°, 60.6° and 66.9° 2-theta) and NiAl$_2$O$_4$ (at 37.2° and 78.5° 2-theta), respectively. For the catalysts prepared with the combined preparation techniques crystallinity of La$_2$O$_3$ and/or La(OH)$_3$ was emphasized by reflexes found at 47.3° and 58.5° 2-theta. Furthermore, no reflections attributable to the NiLa$_2$O$_3$ perovskite-like structure were observed. This comes in good agreement with studies, reporting that high calcination temperature would favor perovskite-like structure formation but also an appropriate ratio of Ni and La is needed.[39]

H$_2$-TPR profiles of the calcined catalysts showed a great variation of the reducibility of the catalysts (Fig. 1). H$_2$ uptake for each catalyst and temperature range was calculated and presented in Table 3. Concerning Ni-based catalysts supported on γ-Al$_2$O$_3$, 4 different species with increasing reduction temperature have been reported: Ni-α species [300–500 °C] that correspond to reducing bulk NiO with very low interaction with γ-Al$_2$O$_3$, Ni-β$_1$ species [500–600 °C] that correspond to NiO interacting moderately with γ-Al$_2$O$_3$, Ni-β$_2$ [600–900 °C] that correspond to non-stoichiometric spinel species with strong interaction with the support and finally Ni-γ species [600–900 °C] that correspond to bulk NiAl$_2$O$_4$ species.[40–42] Signals corresponding to reduction of La species did not occur because of the high reduction temperature of lanthanates.[43,44] The results obtained are in reasonable agreement with the reduction temperatures of the different Ni species, though some signals overlap and shift from the reported values. This observation can be attributed to the presence of the textural La-promoter. For catalysts IW3M and SD3M, reduction started at temperatures higher than 650 °C suggesting that only spinel species strongly interacting with the support and no separate NiO were

Table 2 Specific surface area of all seven fresh calcined catalysts (BET method)

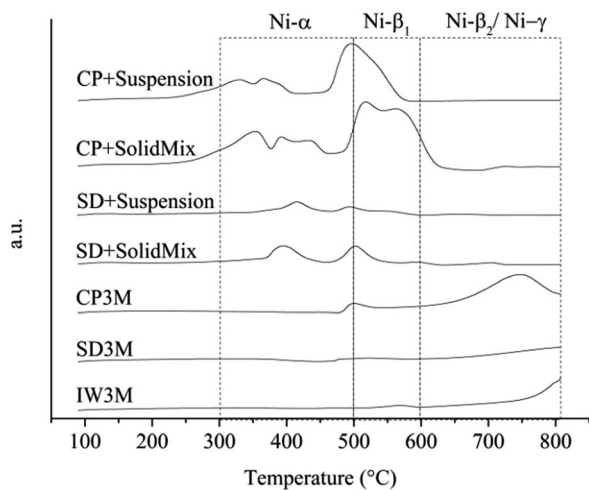|	IW3M	SD3M	CP3M	SD + SolidMix	SD + suspension	CP + SolidMix	CP + suspension
Surface area (m^2 g^{-1})	98.8	9.8	97.0	127.4	138.1	118.3	118.8
Total pore volume (cm^3 g^{-1})	0.42	0.01	0.21	0.41	0.45	0.37	0.37
Average pore size (Å)	102	27	52	94	96	96	95

Fig. 1 H$_2$-TPR profiles.

available. We observed a comparable H$_2$-TPR profile for CP3M; however, also small amounts of reducible NiO species potentially exhibiting a moderate support interaction appear. For SD + SolidMix, SD + suspension, CP + SolidMix and CP + suspension the acquired profiles differ significantly possessing two major peak regions; between 300 and 500 °C signals can be mainly attributed to Ni-α (bulk NiO species), whereas Ni-β$_1$ species – smaller NiO domains moderately interacting with the γ-Al$_2$O$_3$ support – cause signal at temperature of 450 to 620 °C, respectively. Interestingly, these catalysts did not possess species causing high reduction temperatures of above 650 °C. Moreover, the H$_2$-TPR profile of SD + SolidMix differs to some extent from SD + suspension although the NiO and La$_2$O$_3$ species were prepared for both cases in one step by spray drying. This could be attributed to the different preparation technique of introducing γ-Al$_2$O$_3$, physical mixture and ethanol for SolidMix and suspension, respectively.

Elemental mapping (EDX) of the materials facilitated insights into element distribution. Fig. 2 provides an overview of Al, La and Ni for IW3M, CP3M, SD + SolidMix and SD + suspension, respectively. For most catalysts, Ni and La signals overlapped suggesting that La indeed acted as a spacer improving NiO dispersion. IW3M and CP3M exhibited a very good metal dispersion with no obvious nanoparticle formation for NiO. In contrast, for SD + SolidMix and SD + suspension, NiO nanoparticles of around 100 nm in size occurred. For SD3M only STEM images are provided, since only elemental line

measurements were possible due to high charging and instability of the observed specimen (see ESI†). The utilized preparation technique of spray drying led to formation of spherical particles in the size range of 300 to 1500 nm with a good metal dispersion; NiO, La$_2$O$_3$ and Al$_2$O$_3$ were homogeneously dispersed throughout the formed spherical particles. Literature reports suggest that lower reducibility, namely strong metal–support interaction, could be a direct consequence of high metal dispersion and harsh calcination conditions (800 °C for 8 h).[45] This is in good agreement with the H$_2$-TPR profiles and EDX elemental mapping of the freshly calcined catalysts.

3.2. Dry reforming of methane

All materials were tested in DRM in an atmospheric fixed-bed reactor keeping the bed height constant. In order to account for the different catalyst weights, the reaction rates for CO$_2$ and CH$_4$ conversion were calculated. Conversion of CH$_4$ for SD3M was close to equilibrium (>95%). Considering the approach to thermodynamic equilibrium for these values, the reaction rates of CH$_4$ were corrected, by talking into account the reverse reaction as well:[46,47]

$$R_f = \frac{R_{exp.}}{1 - \eta}, \tag{12}$$

$$\eta = \frac{P_{CO}^2 \times P_{H_2}^2}{P_{CH_4} \times P_{CO_2}} \times \frac{1}{K_{eq.}}, \tag{13}$$

where, $R_{exp.}$ is the net reaction rate based on unit catalyst weight (eqn (7)), P_i is the partial pressure of the i component and $K_{eq.}$ is the equilibrium constant ($K_{eq.}$ = 1577, 3 atm^2 for the DRM under 1 atm at 800 °C (ref. 47)).

Fig. 3a shows reaction time courses. The standard error of the measurements (S.E.) was calculated to be 0.02×10^{-5} and 0.01×10^{-5} for the reaction rate of CO$_2$ and CH$_4$, respectively; the reaction rate for CH$_4$ always exceeded the one of CO$_2$ suggesting that reverse water–gas shift (RWGS) reaction (eqn (4)) was disfavored at the utilized reaction conditions (800 °C, CO$_2$: CH$_4$ = 2 : 1, 35 000 h^{-1}). Thermodynamic calculations, assuming $\Delta G° = 0$, showed that 820 °C is the upper limiting temperature for RWGS and 640 °C the lower limiting for DRM.[48] Comparing the yields of H$_2$ and H$_2$O derived from DRM and RWGS, respectively, at different temperatures it was found that the first was the dominant reaction at temperatures higher than 330 °C with a catalytic system that wasn't reported.[49,50]

IW3M, SD3M and CP3M exhibited the best catalytic performance concerning both activity and stability throughout the 6 h

Table 3 H$_2$-uptake of all seven fresh catalysts

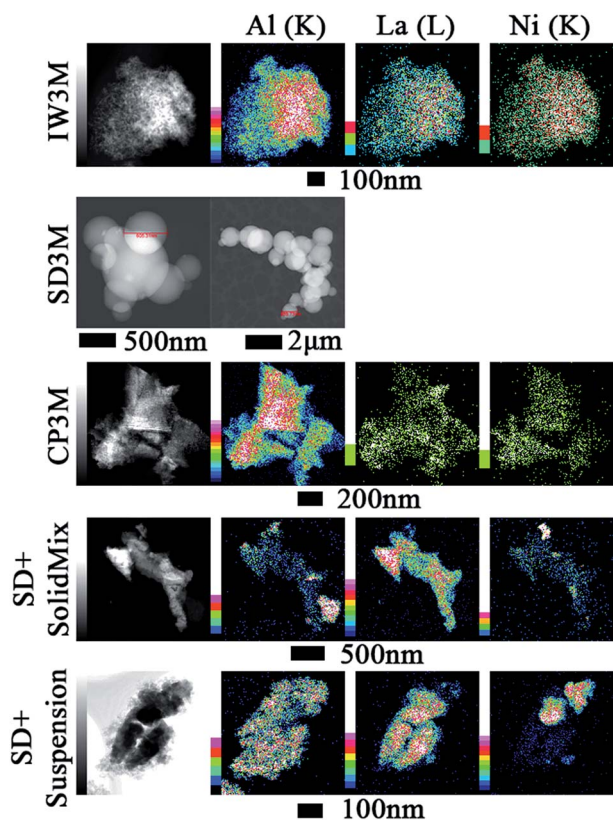|		H$_2$-uptake (mmol H$_2$ g$_{cat}^{-1}$)						
		IW3M	SD3M	CP3M	SD + SolidMix	SD + suspension	CP + SolidMix	CP + suspension
Temperature (°C)	300–500	0.49	0.28	0.20	1.82	1.56	3.47	3.14
	500–600	0.39	0.23	0.50	0.47	0.32	4.02	1.87
	600–800	4.58	1.78	4.41	0.04	0.13	0.28	0.16
	Total	5.46	2.29	5.11	2.32	2.01	7.77	5.17

Fig. 2 EDX elemental mapping of the fresh calcined catalysts. Color scale, to the left of images, represents intensity of correspondent element characteristic X-ray line.

time on stream (TOS). The final reaction rate of CH_4 at 6 h TOS for SD3M was 30.8×10^{-5} mol g_{cat}^{-1} s^{-1}, surpassing the reaction rate of the other two by more than 3 times, 9.5×10^{-5} and 8.3×10^{-5} mol g_{cat}^{-1} s^{-1} for IW3M and CP3M, respectively. In fact, IW3M and SD3M exhibited superior catalytic activity and stability compared to the other catalysts. However, IW3M deactivated over time, whereas SD3M showed stable activity for CO_2 over the studied TOS and increasing activity over the first 4 h TOS for CH_4. Concerning this initial activation of SD3M, incomplete reduction of the catalyst and subsequently further reduction by H_2 derived from CH_4 decomposition was ruled out, since the same observation was true for both 2 and 3 h of catalyst reduction before reaction. A possible explanation could be the structural change of the catalysts at 800 °C, revealing more active sites through Ni-nanoparticle migration, leading to higher activity. In the future, this finding will be further investigated. The four catalysts prepared by the combined techniques displayed inferior catalytic activity and stability. Focusing on the final reaction rates of CH_4 at 6 h TOS, we identified the following ranking of all 7 catalysts:

SD3M > IW3M > CP3M > CP + suspension > CP + SolidMix > SD + suspension > SD + SolidMix.

Different preparation techniques have a strong influence on physico-chemical properties and performance of a catalyst.[51,52] Mesoporous materials are commonly used due to their high surface area and pore volume as well as their uniform pore size leading to more accessible and exposed active sites.[53] This comes in contradiction with our study, where the two worst performing catalysts, SD + SolidMix and SD + suspension,
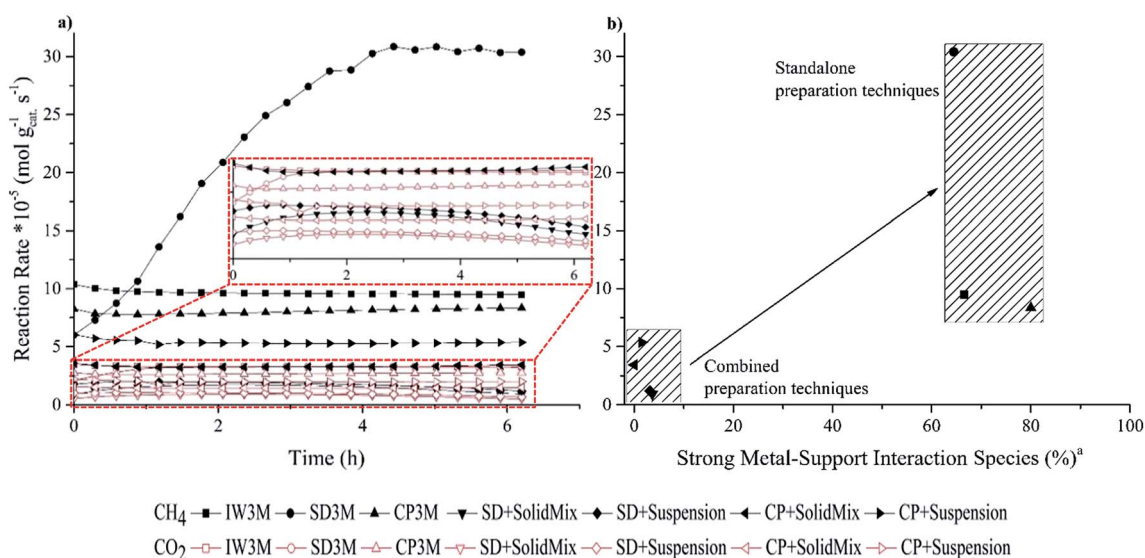

Fig. 3 (a) Reaction rates of CO_2 and CH_4 for the DRM (800 °C, CO_2 : CH_4 = 2 : 1, 10% (v/v) N_2, 35 000 h^{-1}) of all seven catalysts and (b) final reaction rates of CH_4 at 6 h TOS related to the species with strong metal–support interaction. Standard errors (S.E.): S.E. (reaction rate of CH_4) = 0.01×10^{-5} mol g_{cat}^{-1} s^{-1} and S.E. (reaction rate of CO_2) = 0.02×10^{-5} mol g_{cat}^{-1} s^{-1}. R_{CH_4} of SD3M was corrected considering the approach to thermodynamic equilibrium. [a]Strong metal − support interaction species (%) =

$$\frac{\int_{600\,°C}^{900\,°C} H_2\text{-TPR curve}}{\int_{300\,°C}^{500\,°C} H_2\text{-TPR curve} + \int_{500\,°C}^{600\,°C} H_2\text{-TPR curve} + \int_{600\,°C}^{900\,°C} H_2\text{-TPR curve}} \times 100.$$

possessed the highest specific surface area with 127.4 and 138.1 m^2 g^{-1}, respectively. On the other hand, the specific surface area of SD3M was 14-fold lower than the latter with 9.8 m^2 g^{-1}, indicating that achieving high specific surface area was not crucial towards good catalytic performance. An explanation of the observed catalytic behavior of all studied catalysts can be their different reducibility. The first three catalysts, IW3M, SD3M and CP3M, displayed the lowest reducibility especially in the low temperature regions, which points at the very good dispersions of the active metal phase in these materials. This is in good agreement with the TEM investigations of the freshly calcined catalysts (Fig. 2) and literature reports suggesting that the stronger the metal–support interaction, the better the metal dispersion leading to enhanced activity and stability.[45,54] However, the following contradictory point should be noted. Strong metal–support interactions causing low reducibility means that Ni^{2+} is not completely reduced to Ni^0. The latter is considered to be the active site for DRM. Consequently, catalysts with less "reduced" active sites lead to higher activity. This is in line with literature reports, suggesting that mixture of Ni^{2+} and Ni^0 could facilitate higher activity compared to samples only containing Ni^0.[45,55] The reaction rate of CO$_2$ follows the same trend with the one of CH$_4$ and varies from 0.5 to 3.5 × 10^{-5} mol g$_{cat}^{-1}$ s^{-1} among the different catalysts. It is reported that Ni^0 formed by NiAl$_2$O$_4$ spinels, namely species with strong metal–support interaction, could accommodate the spill-over H derived by CH$_4$ decomposition. With the assistance of spilt over H, CO$_2$ dissociation rate could be enhanced leading to differences in CO$_2$ activity.[56]

Despite identical calcination of all catalysts at 800 °C for 8 h, catalysts prepared by the combined techniques possessed significantly lower activity and stability. We relate this observation to phase separation between Ni- and La-oxides during this calcination step and subsequently to the Ni-nanoparticle size. With smaller nanoparticle size better activity and anti-coking properties were achieved.[57–59] As confirmed by EDX mapping, individual domains of Ni-rich matter are easily distinguishable. These Ni-rich domains are reduced at lower temperatures (Fig. 1) and lead to formation of bigger agglomerates (Fig. 2) during DRM causing more pronounced coking. In line, higher reducibility suggests weaker metal–support interaction associated to the formation of bigger Ni nanoparticles due to sintering during DRM. The bigger the Ni nanoparticles the lower are the observed coke resistance and catalytic activity, respectively. In order to further point this relationship out, we plotted the final reaction rates of CH$_4$ conversion over the amount of species with strong metal–support interaction (%) for all seven catalysts (Fig. 3b). The trend indicates that the higher the amount of strong metal–support interactions the higher catalytic activity. Two groups of catalyst preparation techniques can be distinguished: (a) standalone preparation techniques (IW3M, SD3M, CP3M) that exhibited superior catalytic results and (b) combined preparation techniques (SD + SolidMix, SD + suspension, CP + SolidMix, CP + suspension) with inferior catalytic results. In a comparative study between two Ce-promoted catalysts prepared by co-impregnation and sequential impregnation, the first was found to perform better
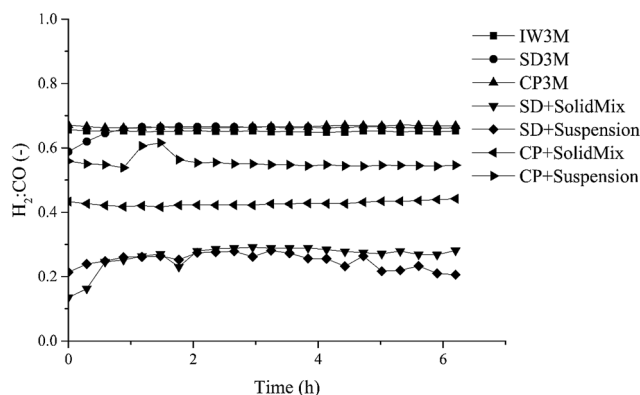

Fig. 4   H$_2$: CO ratio of all seven catalysts.

towards DRM. This was attributed to closer interaction between promoter and active metal, increasing the redox properties of the catalyst.[60] Similarly, for the catalysts prepared by the single preparation technique La, Ni and Al$_2$O$_3$ exhibited stronger interaction than the ones by the combined preparation techniques, leading to better activity and stability.

Selectivities of both H$_2$ and CO (based on total carbon feed, CO$_2$ + CH$_4$) are presented in ESI.† The calculated standard error of the former is 0.17 and for the latter 0.35, respectively. Indeed, the selectivity of H$_2$ varies significantly with the catalysts type. Catalysts prepared with combined preparation techniques exhibited the lowest values compared to IW3M, SD3M and CP3M. The difference in H$_2$ selectivity could be attributed to RWGS and the Boudouard reaction. Reaction rate of CH$_4$ was always higher than the one of CO$_2$ (see ESI†). For the catalysts prepared by a single technique as well as SD + SolidMix and SD + suspension selectivity of hydrogen was higher than the one of CO, indicating that RWGS occurs at a greater extent than the Boudouard reaction. The opposite is suggested for CP + SolidMix and CP + suspension. For CO selectivity, all catalysts possessed stable values at around 50% with the only exception of SD + suspension, which started at 40.3%, increased slightly and then decreased to 42.4% at 6 h TOS. The utilized feed ratio of CO$_2$: CH$_4$ = 2 : 1 could provide a rationale for the stable value of CO selectivity at around 50% but further investigations are needed to better understand this observation.

Focusing on syngas composition (H$_2$: CO) (Fig. 4), catalysts prepared by the standalone techniques (IW3M, SD3M, CP3M) exhibited the highest values of *ca.* 0.65 as opposed to catalysts prepared by combined techniques (CP+*, SD+*). The latter showed relatively low values of the H$_2$: CO ratio of about 0.20–0.55, indicating that the RWGS takes place at a higher extent. This is surprising, since RWGS is thermodynamically limited to 820 °C.[48] Further studies will aim at an understanding of DRM and RWGS over these materials. H$_2$: CO ratio in the absence of carbon deposits and C$_2^+$ should follow the formula;[61]

$$\frac{H_2}{CO} = \frac{3 - R_{CO_2}/R_{CH_4}}{1 + R_{CO_2}/R_{CH_4}}, \qquad (14)$$

where R_{CH_4} and R_{CO_2} are the apparent rates of CH$_4$ and CO$_2$ conversion, respectively. For the single preparation technique
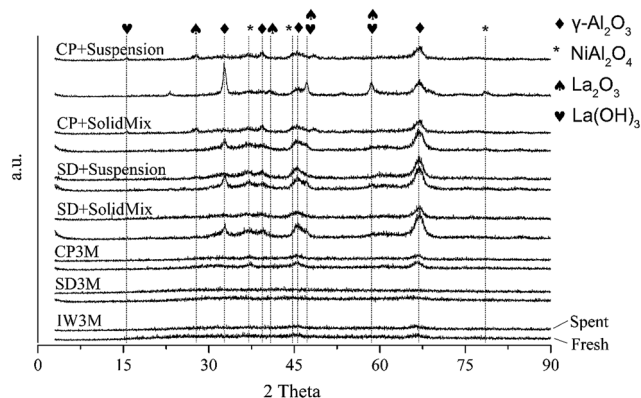
Fig. 5 XRD patterns of all fresh and spent catalysts.

catalysts, we found that the ratio based on stoichiometry was 3-fold greater than the experimental one. For the combined preparation technique catalysts, the stoichiometric-based ratio was 3.5- to 7-fold greater. The reason for this deviation from the stoichiometric ratio would be coke deposition which occurs on all catalysts.

3.3. Spent catalyst characterization

XRD analysis after catalytic reactions showed no change of crystallinity for IW3M, SD3M and CP3M compared to the fresh materials (Fig. 5). Interestingly, catalysts based on combined preparation techniques such as CP+* and SD+* exhibited lower crystallinity, especially of the γ-Al$_2$O$_3$ phase. This could be attributed to partial phase transition of γ-Al$_2$O$_3$ to α-Al$_2$O$_3$. In line, reflections related to γ-Al$_2$O$_3$ at 32.5° and 45.8° 2-theta possessed less intensity compared to the fresh materials. At the same time the reflex at 67.1° retained similar intensity suggesting a potential preferential orientation. Less intense NiAl$_2$O$_4$ reflections were found at 36.7° and 44.5° for all spent catalysts. A possible explanation can be the *in situ* reduction of NiAl$_2$O$_4$ domains to metallic Ni before reaction. It should be noted that no NiO reflections were identified for both fresh and spent catalysts although NiO species were detected by H$_2$-TPR for all fresh catalysts. This indicates small NiO domains not detectable by XRD.

TGA/DSC analyses in air enabled investigating carbon formation on all seven spent catalysts (Table 4 and see ESI†). Focusing on DSC, exothermic events corresponding to oxidation of different carbon species became evident at different temperatures. DSC signals at 300 to 500 °C and at 550 to 700 °C

were related to amorphous and graphitic carbon oxidation, respectively.[62–64]

Firstly, amorphous carbon is formed and then, depending on the reaction conditions and the catalytic system, graphitization gradually occurs converting amorphous to graphitic carbon. All seven spent catalysts demonstrated the existence of at least some amount of amorphous carbon. The amount of graphitic carbon varies throughout the catalysts with CP3M exhibiting the highest amount of all seven spent catalysts. SD3M and SD + suspension presented moderate amounts, while the rest of the catalysts exhibited very low or no graphitic carbon. The weight loss due to carbon oxidation was also measured and translated to percentage of carbon deposits. The best performing catalysts, IW3M and SD3M, presented relatively low amounts of carbon at 3.9 and 2.7%, respectively. This is in good agreement with literature reports, suggesting that homogeneity of active sites, as it was confirmed by EDX elemental mapping, could sharply decrease carbon deposits.[31] Carbon could be gasified either by O* derived by CO$_2$ decomposition or by H$_2$O produced by RWGS leading to less carbon deposits after reaction. The later is mainly met in steam reforming of methane but with the presence of the produced water during DRM, this is expected to lower the amount of carbon deposits for IW3M and SD3M.[65,66]

CP3M exhibited the highest amount of carbon of all seven spent catalysts with 14.4%. The catalysts with combined preparation techniques showed relatively low amounts of carbon deposits. CP + SolidMix had practically no carbon deposits, although it exhibited moderate reaction rates compared to the other catalysts indicating carbon free operation at the given reaction conditions. SD + SolidMix and SD + suspension possessed very low activity but relatively high amounts of coke deposits. A possible explanation could be that they started with higher activity that lead to coking and deactivated rapidly before sampling from the online GC.

Further, investigating carbon deposits on all spent catalysts, we found that the higher the amount of strong metal–support interacting species on the fresh catalyst, found by H$_2$-TPR analysis, the less the amount of coke deposits (%) (Fig. 6a). CP + SolidMix exhibited a minimal amount of coke deposits (%) as the reaction rates were also minimal. CP3M had at the same time significantly higher values of both. For the mentioned correlation, we considered these extreme points as outliers. Also, a trend of the nature of the carbon deposits could be identified; the higher the amount of coke deposits (%) the higher the graphitization degree (Fig. 6b). Again, CP3M was not considered for the correlation.

Table 4 TGA/DSC analysis of all seven spent catalysts

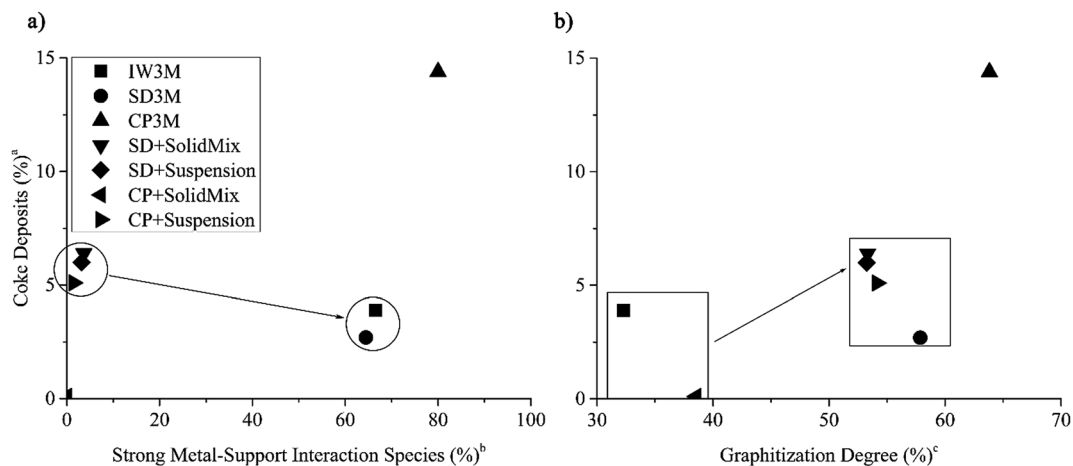|	IW3M	SD3M	CP3M	SD + SolidMix	SD + suspension	CP + SolidMix	CP + suspension
Mass loss (%)	3.9	2.7	14.4	6.4	6.0	0.1	5.1
Temperature (°C)[a]	300	650	300, 600	500	500	350	350, 600
Carbon species	Amorphous	Graphitic	Amorphous graphitic	Amorphous	Amorphous	Amorphous	Amorphous graphitic

[a] Temperature of DSC peaks.

Fig. 6 (a) Amount of coke deposits in percentage in spent catalyst over the amount of species with strong metal–support interaction in the fresh catalyst in percentage and (b) amount of coke deposits in percentage over the graphitization degree in all seven spent catalysts. (CP3M has been excluded from the correlation). [a]Coke deposits (%) = 100%-TGA mass loss (%) at 1000 °C.

$$^{b}\text{Strong metal} - \text{support interaction species (\%)} = \frac{\int_{600\,°C}^{900\,°C} H_2\text{-TPR curve}}{\int_{300\,°C}^{500\,°C} H_2\text{-TPR curve} + \int_{500\,°C}^{600\,°C} H_2\text{-TPR curve} + \int_{600\,°C}^{900\,°C} H_2\text{-TPR curve}} \times 100.$$ [c]Graphitization

$$\text{degree (\%)} = \frac{\int_{550\,°C}^{800\,°C} \text{DSC curve}}{\int_{300\,°C}^{500\,°C} \text{DSC curve} + \int_{550\,°C}^{800\,°C} \text{DSC curve}} \times 100.$$

In Fig. 7 the results of the STEM-EDX elemental mapping are presented for five spent catalysts. It is clear that sintering occurs during DRM leading to bigger nanoparticles of Ni for IW3M and CP3M. For these two catalysts, the metal dispersion was very high with no distinguishable Ni particles before reaction. However, after reaction, we observed nanoparticles of 15–70 nm
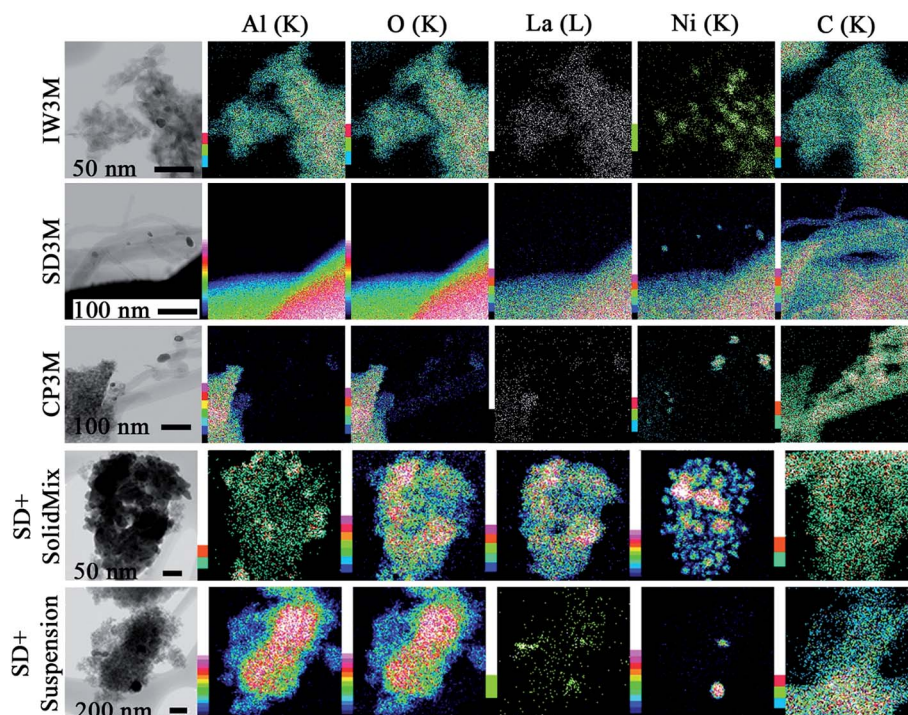

Fig. 7 EDX elemental mapping of the spent catalysts. Color scale, to the left of images, represents intensity of correspondent element characteristic X-ray line.
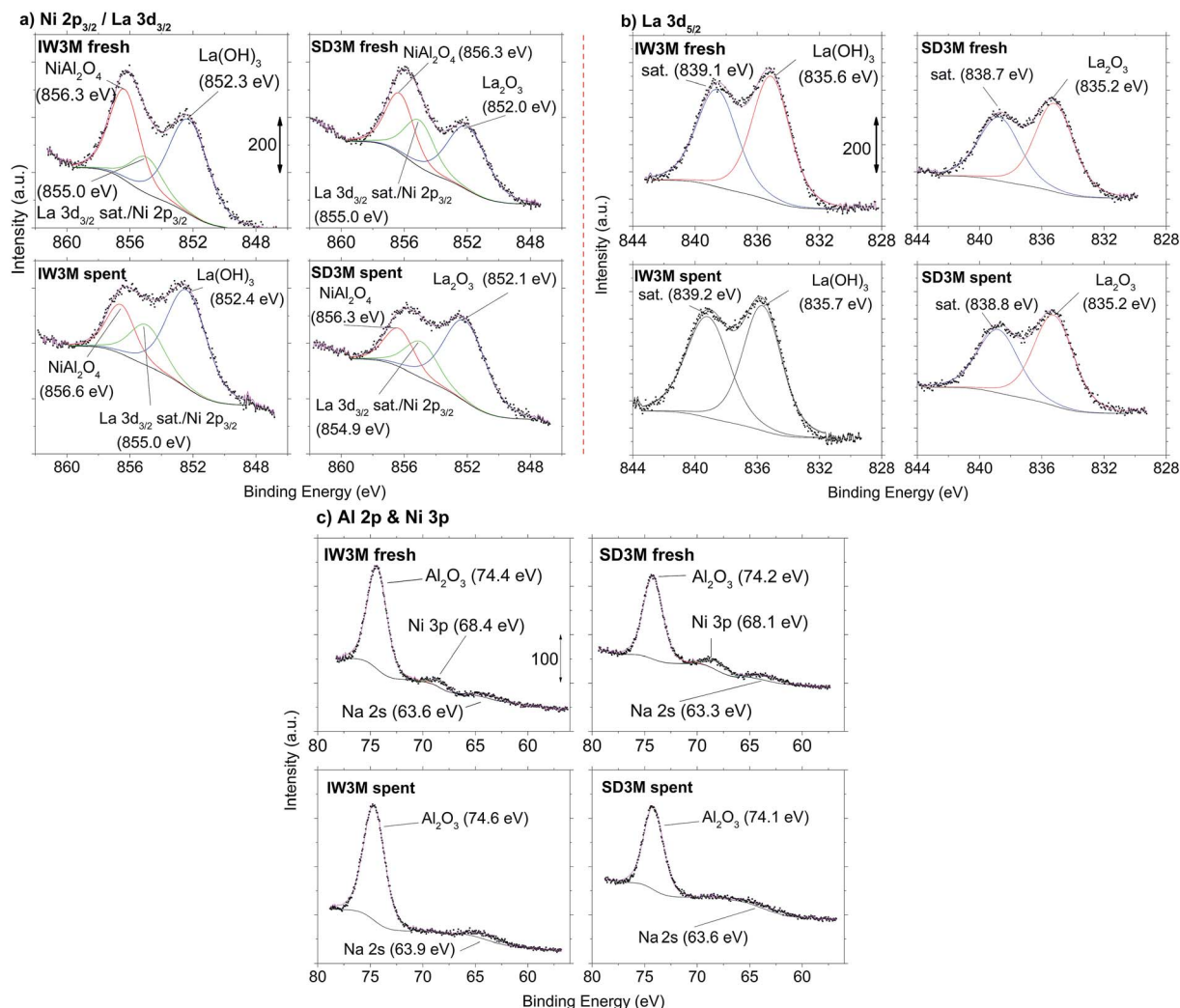
Fig. 8 XPS spectra of IW3M and SD3M prior (fresh) and after reaction (spent). (a) Ni $2p_{3/2}$- and La $3d_{3/2}$-signals (b) La $3d_{5/2}$-signals and (c) Al 2p- and Ni 3p-signals.

size. SD + SolidMix and SD + suspension displayed the same big Ni-rich domains as observed for the fresh catalysts. No carbon filaments formed for these two materials. Most probably, the nature of the preparation procedure played a crucial role for this behavior; lanthanum and nickel segregated during the first calcination step forming separate domains of NiO and La containing species. We assume that La is present in the form of La_2O_3. La_2O_3 in close proximity of the DRM active Ni-rich domains is known to possess high oxidation potential with respect to deposited surface carbon species.[21] Therefore, no carbon nanotubes could be observed for SD + SolidMix and SD + suspension. In practice, for the mixed preparations, we obtained La_2O_3-supported Ni catalysts, where the third phase, γ-Al_2O_3, is considered to be only a spectator. SD3M exhibited no visible large scale sintering; only some small Ni particles (less than 10 nm in size) were found on the tips of the carbon filaments (Fig. 7). These particles are most probably detached from the support during reaction, suggesting that some small scale phase segregation occurred. This observation is in line with the

suggested growth mechanism of carbon nanotubes, where carbon, derived mainly from CH_4 dissociation, migrates through the Ni nanoparticle to precipitate at the nickel–support interface. This interfacial carbon built-up pushes the isolated Ni-particles away from the support leading eventually to its deactivation.[67] Focusing on the carbon species formed, the STEM results are in reasonable agreement with the ones from TGA/DSC, where for CP3M and SD3M (the catalysts with the highest graphitization degree) carbon nanotubes were found. For the rest of the catalysts with low graphitization degree no carbon nanotubes were observed.

The surface chemistry of IW3M and SD3M, the two best performing catalysts, was investigated for both, fresh and spent catalysts by means of XPS analysis (Fig. 8). The most significant difference in surface chemistry between the two catalysts lies in the chemical state of La which was probed by the La $3d_{5/2}$ signal (Fig. 8b). Deconvoluted signals of IW3M, for both fresh and spent catalysts, are located at 835.6 eV and attributed to the formation of $La(OH)_3$.[68] In contrast, the main La $3d_{5/2}$-signal of

the fresh and spent SD3M catalyst is positioned at 0.4 eV lower binding energy consistent with the formation of La_2O_3.[68] The Ni $2p_{3/2}$ signal (Fig. 8a) overlaps with the La $3d_{3/2}$ signal. However, peaks at 856.3 and 856.6 eV clearly indicate the formation of $NiAl_2O_4$ for both the fresh and spent catalysts,[69–72] while a signals 854.9–855.0 eV may originate from the La $3d_{3/2}$ satellite signal[68] and/or the Ni $2p_{3/2}$-signal which could indicate the formation of NiO.[70–72] While for all examined powders the XPS analysis remains inconclusive regarding the potential formation of NiO due to the overlap with the La satellite signal, the formation of $NiAl_2O_4$ is evident. Furthermore, the intensity of signals associated with the presence of $NiAl_2O_4$ is clearly reduced for the spent catalysts as compared to the fresh state. The Ni 3p signal detected at 68.4 eV and 68.1 eV (Fig. 8c) for the fresh catalysts IW3M and SD3M cannot be detected in the spent state for both materials, indicating a Ni depletion consistent with the concomitant reduction in signal associated with the presence of $NiAl_2O_4$. Finally, the Al 2p signals (Fig. 8c) detected at 74.1–74.6 eV for all samples investigated are attributed to the formation of Al_2O_3.[69,72,73] It is reasonable to assume that the detected Na was incorporated during storage of the sample in air prior to the XPS analysis.

4. Summary and conclusion

La promoted Ni/γ-Al_2O_3 catalysts were synthesized by seven different preparation techniques. All catalysts were tested in 6 h catalytic experiments of methane dry reforming (DRM). Additionally, the materials were extensively characterised before and after reaction. Three catalysts were prepared in a single step with all constituents present: incipient wetness impregnation, spray drying, co-precipitation denoted as IW3M, SD3M and CP3M, respectively. Four other catalysts were synthesized by combined techniques: spray drying-physical mixture, spray drying-ethanol suspension, coprecipitation–physical mixture and coprecipitation–ethanol suspension, denoted as SD + SolidMix, SD + suspension, CP + SolidMix and CP + suspension, respectively. The total surface area of all catalysts measured by the BET method was in the same order of magnitude with the exception of SD3M which displayed much lower surface area. XRD patterns showed overall low crystallinity for all catalysts, despite calcination at 800 °C. Additionally, XRD analyses confirmed the presence of γ-Al_2O_3 and NiO for almost all calcined catalysts, and metallic Ni for some of the spent materials. Interestingly, lanthana was not found by XRD, suggesting a high dispersion of this phase. Most probably the same argument explains the difficulty to clearly distinguish the Ni-containing phases for some catalysts. H_2-TPR profiles revealed generally four Ni species with low, moderate and strong metal–support interactions. IW3M, SD3M and CP3M exhibited mainly Ni species with strong metal–support interaction facilitating very good metal dispersions, with SD3M exhibiting the highest amount of strongly interacting Ni species. Catalytic results revealed that single-step preparation techniques provided catalysts exhibiting better reaction rates for both CO_2 and CH_4 conversions. SD3M showed superior activity and stability even outperforming IW3M. Selectivity to CO was stable at around

50% for all seven catalysts except SD + suspension displaying much lower CO selectivity. On the other hand, H_2 selectivities were quite different among the examined catalysts, with SD3M displaying the highest. XRD analysis of the spent catalysts demonstrated an overall decrease of crystallinity after catalysis. Investigating further the carbon deposits formed, TGA/DSC analysis revealed different level of graphitization for all catalysts after reaction, with CP3M demonstrating the highest amount of graphitic and total carbon. Additionally, the presence of $NiAl_2O_4$ on the catalysts surface could be identified by XPS, while depletion of surface Ni was observed for spent catalysts. EDX elemental mapping of the spent catalysts showed that sintering occurred for IW3M and CP3M. SD3M retained its excellent metal dispersion after reaction, whereas only some small nanoparticles of Ni were detached from the support due to carbon nanotube growth. It exhibited the best catalytic results for DRM, addressing sintering which is considered to be one of the main deactivation mechanisms.

Catalyst prepared by spray drying, namely SD3M, showed superior catalytic results irrespective of its low specific surface area compared to materials prepared *via* more conventional techniques. This superior performance can be attributed to excellent Ni dispersion and strong metal–support interactions leading to very low formation of carbon deposits. These properties also facilitate very stable catalytic activity. In line, catalyst morphology remains intact in the course of the reaction for 6 h time-on-stream in DRM. Overall, spray drying appears promising to further improve the performance of catalysts for DRM. Future studies will focus on optimized spray drying conditions aiming for even higher nickel dispersion, further enhanced metal–support interactions and materials possessing high specific surface areas.

Conflicts of interest

There are no conflicts to declare.

Acknowledgements

References

1 J. R. H. Ross, *Catal. Today*, 2005, **100**, 151–158.
2 M. Sohrabi, N. I. Kechut, M. Riazi, M. Jamiolahmady, S. Ireland and G. Robertson, *Transp. Porous Media*, 2011, **91**, 101–121.
3 H. Lei, S. Yang, L. Zu, Z. Wang and Y. Li, *Energy Fuels*, 2016, **30**, 8922–8931.
4 M. Younas, M. Sohail, L. K. Leong, M. J. Bashir and S. Sumathi, *Int. J. Environ. Sci. Technol.*, 2016, **13**, 1839–1860.

5 J. H. Bitter, K. Seshan and J. A. Lercher, *Top. Catal.*, 2000, **10**, 295–305.

6 J. Galuszka, R. N. Pandey and S. Ahmed, *Catal. Today*, 1998, **46**, 83–89.

7 M.-S. Fan, A. Z. Abdullah and S. Bhatia, *ChemCatChem*, 2009, **1**, 192–208.

8 S. Kawi, Y. Kathiraser, J. Ni, U. Oemar, Z. Li and E. T. Saw, *ChemSusChem*, 2015, **8**, 3556–3575.

9 S. Li and J. Gong, *Chem. Soc. Rev.*, 2014, **43**, 7245–7256.

10 C. Carrara, J. Múnera, E. A. Lombardo and L. M. Cornaglia, *Top. Catal.*, 2008, **51**, 98–106.

11 P. Ferreira-Aparicio, C. Márquez-Alvarez, I. Rodríguez-Ramos, Y. Schuurman, A. Guerrero-Ruiz and C. Mirodatos, *J. Catal.*, 1999, **184**, 202–212.

12 J. Kehres, J. G. Jakobsen, J. W. Andreasen, J. B. Wagner, H. Liu, A. Molenbroek, J. Sehested, I. Chorkendorff and T. Vegge, *J. Phys. Chem. C*, 2012, **116**, 21407–21415.

13 K. Sutthiumporn and S. Kawi, *Int. J. Hydrogen Energy*, 2011, **36**, 14435–14446.

14 Z. L. Zhang, X. E. Verykios, S. M. MacDonald and S. Affrossman, *J. Phys. Chem.*, 1996, **100**, 744–754.

15 P. Chen, Z. Hou, X. Zheng and T. Yashima, *React. Kinet. Catal. Lett.*, 2005, **86**, 51–58.

16 Y. K. Han, C.-I. Ahn, J.-W. Bae, A. R. Kim and G. Y. Han, *Ind. Eng. Chem. Res.*, 2013, **52**, 13288–13296.

17 Z. Xu, Y. M. Li, J. Y. Zhang, L. Chang, R. Q. Zhou and Z. T. Duan, *Appl. Catal., A*, 2001, **210**, 45–53.

18 J. Zhang, H. Wang and A. K. Dalai, *J. Catal.*, 2007, **249**, 300–310.

19 G. S. Gallego, C. Batiot-Dupeyrat, J. Barrault, E. Florez and F. Mondragon, *Appl. Catal., A*, 2008, **334**, 251–258.

20 G. S. Gallego, F. Mondragón, J. Barrault, J.-M. Tatibouët and C. Batiot-Dupeyrat, *Appl. Catal., A*, 2006, **311**, 164–171.

21 J.-K. Xu, K.-W. Ren, X.-L. Wang, W. Zhou, X.-M. Pan and J.-X. Ma, *Acta Phys.-Chim. Sin.*, 2008, **24**, 1568–1572.

22 S. Damyanova and J. M. C. Bueno, *Appl. Catal., A*, 2003, **253**, 135–150.

23 M. Schmal, M. M. V. M. Souza, V. V. Alegre, M. A. P. da Silva, D. V. César and C. A. C. Perez, *Catal. Today*, 2006, **118**, 392–401.

24 H.-S. Roh, H. S. Potdar and K.-W. Jun, *Catal. Today*, 2004, **93–95**, 39–44.

25 R. Martínez, E. Romero, C. Guimon and R. Bilbao, *Appl. Catal., A*, 2004, **274**, 139–149.

26 Å. Slagtern, U. Olsbye, R. Blom, I. M. Dahl and H. Fjellvåg, *Appl. Catal., A*, 1997, **165**, 379–390.

27 B. S. Liu and C. T. Au, *Appl. Catal., A*, 2003, **244**, 181–195.

28 X. E. Verykios, *Int. J. Hydrogen Energy*, 2003, **28**, 1045–1063.

29 S. Tang, L. Ji, J. Lin, H. C. Zeng, K. L. Tan and K. Li, *J. Catal.*, 2000, **194**, 424–430.

30 H. Y. Wang and E. Ruckenstein, *Carbon*, 2002, **40**, 1911–1917.

31 J.-g. Wang, C.-j. Liu, Y.-p. Zhang, K.-l. Yu, X.-l. Zhu and F. He, *Catal. Today*, 2004, **89**, 183–191.

32 H. A. Aleksandrov, N. Pegios, R. Palkovits, K. Simeonov and G. N. Vayssilov, *Catal. Sci. Technol.*, 2017, **7**(15), 3339–3347.

33 Y.-x. Pan, C.-j. Liu, T. S. Wiltowski and Q. Ge, *Catal. Today*, 2009, **147**, 68–76.

34 R. Zhao, S. J. Lee, I. H. Son, H. Lee and A. Soon, *Appl. Surf. Sci.*, 2013, **265**, 339–345.

35 K. Mette, S. Kühl, H. Düdder, K. Kähler, A. Tarasov, M. Muhler and M. Behrens, *ChemCatChem*, 2014, **6**, 100–104.

36 J. W. Han, C. Kim, J. S. Park and H. Lee, *ChemSusChem*, 2014, **7**, 451–456.

37 B. A. Latella and B. H. O'Connor, *J. Am. Ceram. Soc.*, 1997, **80**, 2941–2944.

38 T. C. Chou, D. Adamson, J. Mardinly and T. G. Nieh, *Thin Solid Films*, 1991, **205**, 131–139.

39 S. M. de Lima, A. M. da Silva, L. O. O. da Costa, J. M. Assaf, G. Jacobs, B. H. Davis, L. V. Mattos and F. B. Noronha, *Appl. Catal., A*, 2010, **377**, 181–190.

40 F. Bentaleb and E. Marceau, *Microporous Mesoporous Mater.*, 2012, **156**, 40–44.

41 J. M. Rynkowski, T. Paryjczak and M. Lenik, *Appl. Catal., A*, 1993, **106**, 73–82.

42 R. Yang, X. Li, J. Wu, X. Zhang, Z. Zhang, Y. Cheng and J. Guo, *Appl. Catal., A*, 2009, **368**, 105–112.

43 B. Valle, B. Aramburu, A. Remiro, J. Bilbao and A. G. Gayubo, *Appl. Catal., B*, 2014, **147**, 402–410.

44 X. Wang, Y. Wei, J. Zhang, H. Xu and W. Li, *React. Kinet. Catal. Lett.*, 2006, **89**, 97–104.

45 S. Damyanova, B. Pawelec, K. Arishtirova and J. L. G. Fierro, *Int. J. Hydrogen Energy*, 2012, **37**, 15966–15975.

46 J. Wei and E. Iglesia, *J. Catal.*, 2004, **225**, 116–127.

47 L. N. Bobrova, A. S. Bobin, N. V. Mezentseva, V. A. Sadykov, J. W. Thybaut and G. B. Marin, *Appl. Catal., B*, 2016, **182**, 513–524.

48 S. Wang, G. Lu and G. J. Millar, *Energy Fuels*, 1996, **10**, 896–904.

49 M. C. Bradford and M. A. Vannice, *J. Catal.*, 1998, **173**, 157–171.

50 M. C. J. Bradford and M. A. Vannice, *Catal. Rev.: Sci. Eng.*, 1999, **41**, 1–42.

51 F. Menegazzo, M. Signoretto, F. Pinna, P. Canton and N. Pernicone, *Appl. Catal., A*, 2012, **439**, 80–87.

52 D.-W. Jeong, W.-J. Jang, J.-O. Shim, H.-S. Roh, I. H. Son and S. J. Lee, *Int. J. Hydrogen Energy*, 2013, **38**, 13649–13654.

53 M. E. Davis, *Nature*, 2002, **417**, 813–821.

54 Y.-g. Chen and J. Ren, *Catal. Lett.*, 1994, **29**, 39–48.

55 R. Wang, H. Xu, X. Liu, Q. Ge and W. Li, *Appl. Catal., A*, 2006, **305**, 204–210.

56 Z. X. Cheng, X. G. Zhao, J. L. Li and Q. M. Zhu, *Appl. Catal., A*, 2001, **205**, 31–36.

57 A. G. Bhavani, W. Y. Kim, J. Y. Kim and J. S. Lee, *Appl. Catal., A*, 2013, **450**, 63–72.

58 L. Sun, Y. Tan, Q. Zhang, H. Xie, F. Song and Y. Han, *Int. J. Hydrogen Energy*, 2013, **38**, 1892–1900.

59 V. Y. Bychkov, Y. P. Tyulenin, A. A. Firsova, E. A. Shafranovsky, A. Y. Gorenberg and V. N. Korchak, *Appl. Catal., A*, 2013, **453**, 71–79.

60 Ş. Özkara-Aydınoğlu, E. Özensoy and A. E. Aksoylu, *Int. J. Hydrogen Energy*, 2009, **34**, 9711–9722.

61 M. C. J. Bradford and M. A. Vannice, *J. Catal.*, 1999, **183**, 69–75.

62 S. de Llobet, J. L. Pinilla, R. Moliner and I. Suelves, *Fuel*, 2015, **139**, 71–78.

63 L. Mo, K. K. M. Leong and S. Kawi, *Catal. Sci. Technol.*, 2014, **4**, 2107–2114.

64 X. Yu, N. Wang, W. Chu and M. Liu, *Chem. Eng. J.*, 2012, **209**, 623–632.

65 S. Wang, G. Q. Lu and G. J. Millar, *Energy Fuels*, 1996, **10**, 896–904.

66 L. Maier, B. Schädel, K. Herrera Delgado, S. Tischer and O. Deutschmann, *Top. Catal.*, 2011, **54**, 845.

67 H. Liu, C. Guan, X. Li, L. Cheng, J. Zhao, N. Xue and W. Ding, *ChemCatChem*, 2013, **5**, 3904–3909.

68 M. Sunding, K. Hadidi, S. Diplas, O. Løvvik, T. Norby and A. Gunnæs, *J. Electron Spectrosc. Relat. Phenom.*, 2011, **184**, 399–409.

69 P. Bolt, E. Ten Grotenhuis, J. Geus and F. Habraken, *Surf. Sci.*, 1995, **329**, 227–240.

70 S. Velu, K. Suzuki, M. Vijayaraj, S. Barman and C. S. Gopinath, *Appl. Catal., B*, 2005, **55**, 287–299.

71 I. Pettiti, D. Gazzoli, P. Benito, G. Fornasari and A. Vaccari, *RSC Adv.*, 2015, **5**, 82282–82291.

72 N. Pegios, G. Schroer, K. Rahimi, R. Palkovits and K. Simeonov, *Catal. Sci. Technol.*, 2016, **6**, 6372–6380.

73 M. Giza, P. Thissen and G. Grundmeier, *Langmuir*, 2008, **24**, 8688–8694.